CONDENSED MATTER PHYSICS

Observation of interplay between phonon chirality and electronic band topology

Felix G. G. Hernandez[1]*†, Andrey Baydin[2,3]†, Swati Chaudhary[4,5,6], Fuyang Tay[2,7], Ikufumi Katayama[8], Jun Takeda[8], Hiroyuki Nojiri[9], Anderson K. Okazaki[10]‡, Paulo H. O. Rappl[10], Eduardo Abramof[10], Martin Rodriguez-Vega[4,5], Gregory A. Fiete[5,6], Junichiro Kono[2,3,11,12]*

The recently demonstrated chiral modes of lattice motion carry angular momentum and therefore directly couple to magnetic fields. Notably, their magnetic moments are predicted to be strongly influenced by electronic contributions. Here, we have studied the magnetic response of transverse optical phonons in a set of $Pb_{1-x}Sn_xTe$ films, which is a topological crystalline insulator for $x > 0.32$ and has a ferroelectric transition at an x-dependent critical temperature. Polarization-dependent terahertz magnetospectroscopy measurements revealed Zeeman splittings and diamagnetic shifts, demonstrating a large phonon magnetic moment. Films in the topological phase exhibited phonon magnetic moment values that were larger than those in the topologically trivial samples by two orders of magnitude. Furthermore, the sign of the effective phonon g-factor was opposite in the two phases, a signature of the topological transition according to our model. These results strongly indicate the existence of interplay between the magnetic properties of chiral phonons and the topology of the electronic band structure.

INTRODUCTION

The symmetries of crystals determine many properties of their phonons, such as their selection rules and degeneracies (*1*). Among the possible symmetries, mirror symmetries play a special role: When they are broken, the lattice ions can display circular motion with finite angular momentum (*2*). These modes are called chiral phonons, and recently, they have been the subject of intense research in a large variety of materials and applications (*3*–*16*). In magnetic fields, chiral phonons preferably absorb polarized light of a given handedness, resulting in magnetic circular dichroism (MCD) (*17*–*19*). Furthermore, chiral phonons carry a finite magnetic moment that results in the phonon Zeeman effect, which has been observed in the narrow-gap semiconductor PbTe (*19*), the nonaxial CeF_3 (*20*), and the Dirac semimetal Cd_3As_2 (*21*), with the phonon magnetic moment values ranging from hundredths to several Bohr magnetons.

There are a few mechanisms that can lead to a finite phonon magnetic moment. Recent theoretical reports (*22*–*24*) have proposed that a phonon magnetic moment can arise from the time-dependent electric polarization induced by a laser-driven infrared-active phonon. However, the predicted magnitude of the phonon magnetic moment, which depends on the phonon effective charge and the ion masses, is relatively small compared to recent experimental observations (*19*, *21*). Larger values compatible with experiments can be obtained when electronic contributions are considered (*25*–*27*). In this regard, Ren *et al.* (*28*) proposed a mechanism where the circular motion of a chiral phonon induces an electronic orbital response that contributes to the phonon magnetic moment. Furthermore, Geilhufe (*29*) suggested that the chiral phonon can induce inertial effects on the electrons, which lead to an effective spin-chiral phonon coupling. Therefore, electronic contributions to the phonon magnetic moment open the possibility for the interplay of chiral phonons and electronic topology. However, no experimental evidence has been reported.

Here, we report results of terahertz time-domain spectroscopy (THz-TDS) experiments on the pseudobinary alloy $Pb_{1-x}Sn_xTe$. This material system is known to be a topological crystalline insulator (TCI) for $x > 0.32$ (*30*, *31*) and has exhibited chiral phonons in strong magnetic fields for $x = 0$ (*19*). We studied one sample in the trivial phase ($x = 0.24$) and two samples in the topological phase ($x = 0.42$ and 0.56). For each sample, we observed two anharmonicity-split transverse optical (TO) phonon modes and characterized their magnetic properties at temperatures low enough to place the samples in their ferroelectric phases (*32*, *33*). Both the trivial and topological samples exhibited chiral phonons, as a consequence of being in a ferroelectric phase with broken inversion symmetry. However, across the topological transition, the phonons switched chirality, and the phonon magnetic moment increased by two orders of magnitude. The ferroelectric transition might influence the increased effect. We supplemented our experimental observations with a theoretical model for the phonon magnetic moment arising from the electronic orbital response following (*28*), which captures the phonon chirality switching across the topological transition. Thus, our results indicate a connection between electronic topology and phonon chirality.

[1]Instituto de Física, Universidade de São Paulo, São Paulo, SP 05508-090, Brazil. [2]Department of Electrical and Computer Engineering, Rice University, Houston, TX 77005, USA. [3]Smalley-Curl Institute, Rice University, Houston, TX 77005, USA. [4]Department of Physics, The University of Texas at Austin, Austin, TX 78712, USA. [5]Department of Physics, Northeastern University, Boston, MA 02115, USA. [6]Department of Physics, Massachusetts Institute of Technology, Cambridge, MA 02139, USA. [7]Applied Physics Graduate Program, Smalley-Curl Institute, Rice University, Houston, TX 77005, USA. [8]Department of Physics, Graduate School of Engineering Science, Yokohama National University, Yokohama 240-8501, Japan. [9]Institute for Materials Research, Tohoku University, Sendai 980-8577, Japan. [10]Instituto Nacional de Pesquisas Espaciais, São José dos Campos, SP 12201-970, Brazil. [11]Department of Physics and Astronomy, Rice University, Houston, TX 77005, USA. [12]Department of Materials Science and NanoEngineering, Rice University, Houston, TX 77005, USA.
*Corresponding author. Email: felixggh@if.usp.br (F.G.G.H.); kono@rice.edu (J.K.)
†These authors contributed equally to this work.
‡Present address: Brazilian Nanotechnology National Laboratory, Campinas, SP 13083-100, Brazil.

RESULTS

Phonon modes at zero magnetic field

$Pb_{1-x}Sn_xTe$ is known to exhibit x-dependent ferroelectric and topological phase transitions (*32*, *33*). The existence of the ferroelectric phase is the result of a rhombohedral distortion of the rock salt structure, which breaks the inversion symmetry and leads to a ferroelectric phase transition at an x-dependent critical temperature (T_c) (*34*–*43*); see Fig. 1A. In addition, with increasing x, the electronic bandgap (E_g) decreases until it closes at a critical value (x_c) and the electronic bands invert around the L-points (*32*, *44*), entering the TCI state (*45*–*53*, *54*). The critical concentration x_c is temperature dependent (*32*); see Fig. 1B.

First, to identify the spectral features corresponding to the TO phonons, we performed standard THz-TDS measurements in a transmission geometry (*55*). A transmittance spectrum for the x = 0.42 sample is shown in Fig. 1C at 250 K and zero magnetic field. The minima observed at ~0.9 THz (TO_1) and ~1.6 THz (TO_2) are consistent with two anharmonicity-split optical phonon modes observed in neutron scattering measurements on PbTe (*56*), similar to features observed in $Pb_{1-x}Sn_xSe$ (*57*) and common in all the studied samples; see the Supplementary Materials (*58*). The large widths of the phonon resonances are related to alloy-inherent disorder. In Fig. 1D, the phonon modes red shift, or soften, continuously with decreasing temperature until the temperature reaches T_c. Below T_c, the modes blue shift (or harden) with decreasing temperature but less steep than expected by the Landau theory of ferroelectrics (*59*, *60*), as also reported for materials with degenerate soft phonons (*61*).

The characterization of the ferroelectric phase in our samples is in agreement with the literature and shown in the Supplementary Materials (*58*), as the scope of this report is the phonon magnetic properties. In short, we found that the critical temperature for the ferroelectric phase transition increases from 15 up to 89 K with an increasing Sn concentration across the set of our samples. Similar Γ-point TO phonon behavior has been associated with a ferroelectric transition of the displacive nature for $Pb_{1-x}Sn_xTe$ (*62*) and SnTe (*59*, *63*). Below T_c for all the samples (T < 15 K), the phonon angular momentum, $J^{ph} = \sum_\alpha m_\alpha \mathbf{u}_\alpha \times \partial_t \mathbf{u}_\alpha$, can be nonzero for a crystal without inversion symmetry (*4*). Here, the index α runs over all the atoms in the crystal; $\mathbf{u}_\alpha$ is the phonon displacement vector, and m_α is the phonon mass. This low-temperature condition is maintained in the following discussion, allowing us to probe chiral phonons and access the TCI phase above $x_c \sim 0.32$.

Phonon chirality in magnetic fields

Next, to investigate the magnetic properties of these TO phonons across the topological transition, we applied magnetic fields up to 30 T combined with THz-TDS (*58*, *64*, *65*). Figure 1E shows a schematic of the experiment. While the incident polarization was set in the x direction, we measured both linear components of the transmitted terahertz electric fields with a detection polarizer oriented along the x (E_x) or y direction (E_y). The magnetic field–induced changes at 29.5 T are displayed in Fig. 1 (F and G). The change in the E_x component (ΔE_x) can be clearly seen to contain several oscillations in time, with the oscillation amplitude slightly reduced for the x = 0.56 sample. The magnetic field–induced y component, E_y, is robust and has a few picosecond oscillations that can be reversed by changing the polarity of the magnetic field (B). An E_y component with amplitude comparable to E_x is a clear indication of the existence of phonon chirality, for which a circular right (R)/left (L) basis, $E_{R,L} = (E_x \pm iE_y)/\sqrt{2}$, is more adequate for analysis.

Figure 2 (A to C) shows $E_{R,L}$ in the frequency domain for all samples for different B. The empty (blue) and solid (red) arrows indicate the positions of the transmission minima for the opposite senses of circular polarization. A high degree of MCD is obtained when a transmission minimum occurs for one polarization while the opposite one displays a maximum. The plots show substantial differences in $E_{R,L}$, depending on whether the sample is a trivial insulator or a TCI. Magnetic fields larger than 7.8 T are required to observe a deep minimum in $E_{R,L}$ for x = 0.24. On the other hand, on the TCI side (x = 0.42 and 0.56), $E_{R,L}$ has well-defined deep minima clearly visible for low fields. This implies that a larger

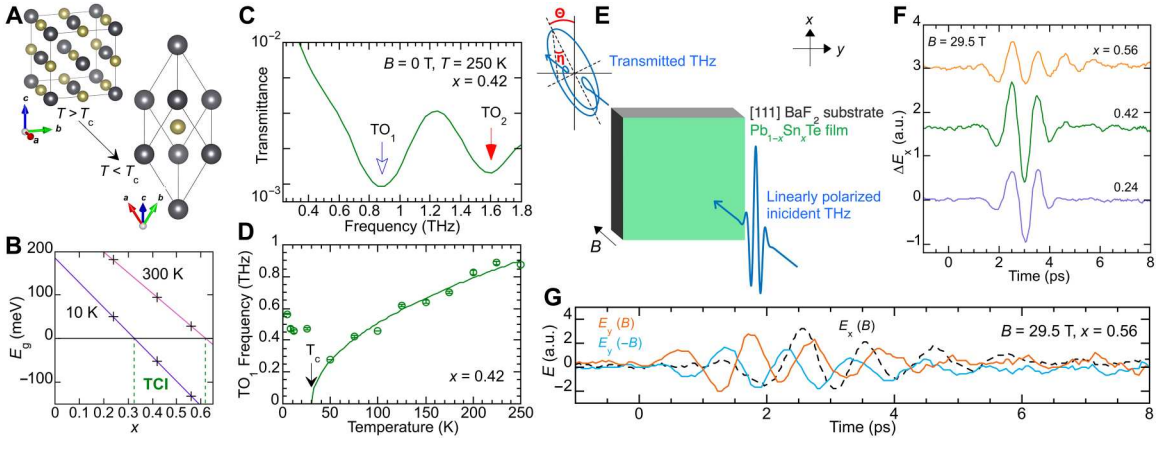

Fig. 1. Magnetic field–induced phonon chirality. (**A**) Cubic and distorted unit cell structure of $Pb_{1-x}Sn_xTe$, where gray spheres represent Pb/Sn atoms and yellow spheres represent Te atoms. (**B**) Diagram of the trivial-to-TCI transition in the 10 to 300 K range, adapted from (*32*). The crosses mark our samples. (**C**) Transmittance at 250 K for x = 0.42 and at B = 0 T. (**D**) Temperature dependence of the frequency of the TO_1 phonon mode for x = 0.42. The solid line is a Curie-Weiss fit. (**E**) Schematic of the experiment showing a linearly polarized terahertz beam at the input and a transmitted beam after passing through the sample in the presence of a perpendicular magnetic field. (**F**) Magnetic field–induced change in E_x at 29.5 T for all samples. (**G**) Transmitted terahertz electric-field E_x and magnetic field–induced E_y components for x = 0.56 at ±29.5 T. a.u., arbitrary units.

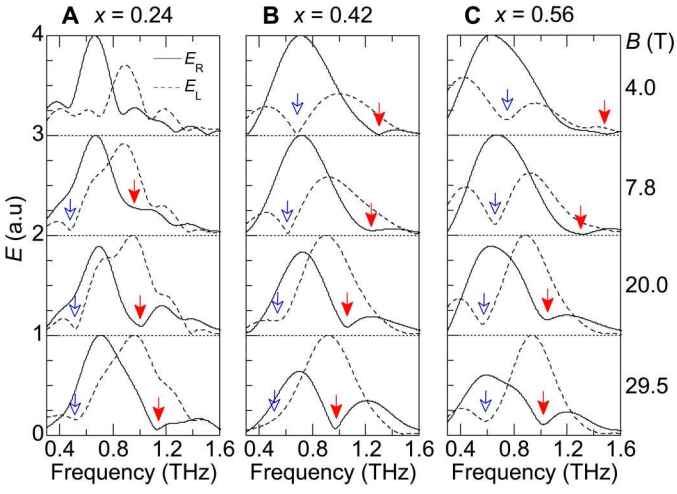

Fig. 2. Phonon magnetic circular dichroism. (**A** to **C**) Right-handed (solid line) and left-handed (dashed line) transmitted electric fields in the frequency domain for several *B*. The data were normalized. The full and empty arrows indicate the position of relevant transmission minima in $E_{R,L}$ as a guide to the eye for the circular dichroism. Scans are vertically offset for clarity. T = 12 K.

degree of MCD can be obtained in the TCI phase, reaching nearly 100% at a much lower B than that needed for the trivial insulator. Note that the MCD value that we recently reported for TO phonons in PbTe (x = 0) at 9 T was 30% (*19*). In addition, while, for the trivial insulator, both polarizations maintain similar amplitudes in the studied field range, for the TCI samples, the dominant transmitted polarization switches from E_R to E_L with increasing B.

We should note that the ferroelectric transition could be responsible for the different degrees of MCD observed in these samples, as broken inversion symmetry is necessary for a finite phonon angular momentum. The x = 0.24 sample at 12 K is close to the ferroelectric transition (12 K/T_c = 0.8), thus leading to undefined phonon circular motion at low B. On the contrary, the samples with higher x are deeper in the ferroelectric phase at the same temperature (12 K/T_c = 0.4 and 0.13 for the x = 0.42 and 0.56 samples, respectively), and the chiral phonons can be obtained at lower magnetic fields.

Giant magnetic moments of phonons in the TCI phase

To quantify the magnetic properties of these chiral phonons, we calculated the complex Faraday rotation (FR) as a function of frequency. While it only relates to the off-diagonal terms of the conductivity tensor, the complex FR allows us to determine the phonon frequencies in the circular basis and has a useful advantage in experiments under extreme conditions: It is not necessary to repeat measurements on the substrate to obtain a reference signal. The real and imaginary parts (FR = Θ + iη) at a given frequency are Θ = [arg(E_R) − arg(E_L)]/2 and η = (|E_L| −|E_R|)/(|E_L| + |E_R|), where Θ is the FR of the polarization plane and η quantifies the ellipticity change (*66*).

Figure 3 (A to C) presents Θ and η for the three samples. For x = 0.24, the signal shows multiple wiggles at low B but exhibits a pair of positive and negative ellipticity peaks and vanishing Faraday rotation at the same frequency in high magnetic fields. Such evolution for the ellipticity is a direct estimate of the MCD, where chiral phonons will lead to the absorption of either |E_R| or |E_L|, resulting in a peak of η = ±1. As argued before for the MCD in the TCI regime, low magnetic fields are sufficient for the appearance of opposite ellipticity peaks together with vanishing FR angles.

Our findings are consistent with previous FR measurements in $Pb_{0.5}Sn_{0.5}Te$ (*49*), which displayed small ellipticity peaks at frequencies similar to ours (although not discussed in their work). In comparison, the lower hole concentrations of our samples allowed us to study the films further into the ferroelectric phase, resulting in clearly one chiral sense per phonon.

The frequencies of the chiral phonons change substantially with the magnetic field strength, as shown in Fig. 3 (D to F). The magnetic properties of the observed phonon branches can be extracted using a model for the quadratic dependence in terms of a Zeeman splitting and diamagnetic shift according to $E_{L,R}(B) = hf_{TO} \pm g^{\star}\mu_B B + \sigma_{dia}B^2$, where h is the Planck constant, f_{TO} is the TO phonon frequency at zero magnetic field, $g^{\star}$ is the effective g-factor, μ_B is the Bohr magneton, and σ_{dia} is the diamagnetic shift coefficient (*19*). We used this equation in Fig. 3 (D to F), as shown by the solid lines, to obtain the parameters plotted in Fig. 3 (G to I).

The trend observed in Fig. 3G for f_{TO}, showing increasing phonon frequencies with x, which is a consequence of the composition-dependent phonon hardening, confirms that all films were below the ferroelectric critical temperature during the experiments in magnetic fields. Note that the x = 0 sample from (*19*) is still in the softening part of the phase transition at that temperature.

For the sample with x = 0.24, the fitting of the Zeeman term for the lowest energy phonon (blue circles in Fig. 3D) gives a value of $g^{\star}$ (0.12 ± 0.02) that is three times larger than that reported for the x = 0 sample (0.043 ± 0.006) (*19*). The large error bar for $g^{\star}$ in this case is mainly a result of the impossibility of fitting the ellipticity peaks down to the low fields. When x is increased into the TCI side, the effective g-factor changes sign for TO_1 and continues to increase with an opposite sign between the two phonon modes, as shown in Fig. 3H. The value of $g^{\star}$ that we obtained for the sample with the largest Sn composition ($g^{\star}$ = −1.2 ± 0.2 for TO_1 and 3.3 ± 0.5 for TO_2) represents a colossal increase, by two orders of magnitude, over the measurements in the trivial insulator samples (x = 0 and 0.24). The order of magnitude is comparable with the value recently reported (2.7) for a soft phonon in the Dirac semimetal Cd_3As_2 (*21*, *67*).

The diamagnetic term, which increases the energies of both chiral branches with an increasing magnetic field, also shows agreement in the order of magnitude between the shift for TO_1 in the x = 0.24 sample and the reported value for x = 0 [(1.9 ± 0.2) × 10^{-4} meV/T^2]. For the same phonon mode, the diamagnetic shift continuously increases by up to one order of magnitude at x = 0.56 [(15 ± 4) × 10^{-4} meV/T^2]. For the TO_2 mode, as seen in the Zeeman term, the value is even larger than that for TO_1 and reaches (39 ± 9) × 10^{-4} meV/T^2.

Because of time reversal symmetry at zero magnetic field, it is expected that each one of the measured phonon modes (TO_1 and TO_2) should produce two circularly polarized branches, perhaps with one weaker branch, as reported for PbTe (*19*), CeF_3 (*20*), and Cd_3As_2 (*21*). Nevertheless, because of strong MCD, only one type of chirality could be experimentally resolved per phonon mode in Fig. 3 (D to F). Furthermore, those single chiral branches acquired opposite handedness, i.e., left-hand (blue) for TO_1 and right-hand (red) for TO_2. Using the obtained fitting parameters, we estimated the position of the minority chiral branches, as

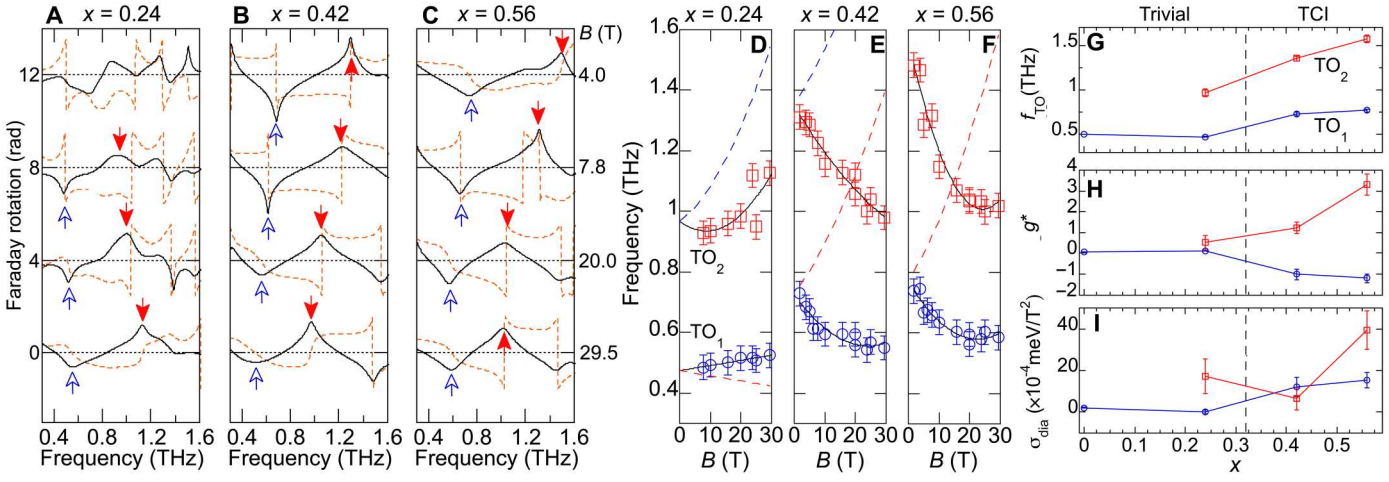

Fig. 3. Phonon magnetic properties across the TCI transition. (**A** to **C**) Θ (dashed lines) and η (solid lines), both in radians, as a function of frequency for several *B*. The arrows indicate the frequencies shown in Fig. 2. (**D** to **F**) Frequency of the ellipticity peaks as a function of *B* with fitting model (solid lines). The dashed lines estimate the position of phonon branches with complementary chirality. The obtained parameters are plotted in (**G** to **I**). The data points for $x = 0$ were extracted from (*19*). Scans shown in (A to C) are vertically offset for clarity. $T = 12$ K.

plotted by the dashed lines. While for $x = 0.24$, those energy branches could be in the unidentified FR features, in the TCI regime, we expect the R-branch for TO_1 to be a shoulder on the low-frequency side of the R-branch for TO_2 where it is hidden by the peak of the dominant chirality for the other phonon. On the other hand, the L-branch for TO_2 should be above its R-branch, which is in the limit or outside the measured frequency window.

DISCUSSION

Now, we discuss possible microscopic mechanisms that give rise to the large effective phonon *g*-factor, $g^\star$, and in particular, the changes observed across the topological transition. Ren *et al.* (*28*) have proposed theoretically a mechanism that leads to phonon effective *g*-factors arising from electronic contributions comparable with the experimental values reported for PbTe (*19*). Within this mechanism, valid when the phonon frequencies are smaller than the electronic bandgap, the circular motion of a chiral phonon induces an electronic orbital response with topological and nontopological contributions that, in turn, give rise to a phonon magnetic moment.

In this work, we adopt a low-energy model for $Pb_{1-x}Sn_xTe$, taking into account the valley degeneracy and the doping present in the samples, and compute the phonon magnetic moment following (*28*); see (*58*) for details. Figure 4A shows a generic electronic band structure for samples with opposite mass terms and Fermi level in the gap. In the trivial phase, we find that this model successfully predicts the increase of the magnetic moment from $x = 0$ to $x = 0.24$, once the occupancy of hole levels in the samples is taken into account, as shown in Fig. 4B. There, we plot the phonon magnetic moment, M_z, as a function of momentum in Fig. 4D. Integrating over momentum, we find the ratio of the magnetic moment at $x = 0.24$ to that at $x = 0$ to be 2.3, which agrees well with the experimental value of 2.8 ± 0.7. The model that we use predicts a sign change of the phonon magnetic moment across the trivial to TCI phases, as observed in our experiments; see Fig. 4C. A $g^\star$-factor sign change has also been predicted across a strong-to-weak topological transition (*28*).

However, our model cannot explain the observed continuous increase of the $g^\star$-factor in the TCI phase. One possible explanation is the different carrier density across the set of samples. However, we found that increasing the carrier density decreases $g^\star$, contrary to the observations (*58*). Another possible explanation is that the surface states contribute to the phonon magnetic moment. However, such a contribution cannot be captured within the premises of our model treating the phonons and electrons consistently (*58*). As the samples with $x > x_c$ are expected to have gapless (111) surface states, an understanding of the enhancement of the phonon magnetic moment should take into account their nonadiabatic contribution. Recently, Geilhufe (*29*) has proposed a mechanism where a chiral phonon mode induces inertial effects in the electrons, leading to an effective spin-chiral phonon coupling that could potentially lead to large phonon magnetic moments. However, the evaluation of this contribution for $Pb_{1-x}Sn_xTe$ requires including the inertial effect Hamiltonian terms in density functional codes. Zhang *et al.* (*68*) have put forward a phonon magnetic moment theory for realistic materials based on first-principles calculations. Both approaches require considering the anharmonic phonon interactions and alloy nature of $Pb_{1-x}Sn_xTe$. In addition, the coupling of the phonons to the electronic cyclotron resonance (*21*) should be negligible, as those are largely detuned for the studied magnetic field range. Although there has been an intense search for topological contributions to phonon effects, as discussed above for (*28*) and in other recent studies (*68*–*71*), further theoretical work is still necessary to fully understand the magnetic moment of phonons in the topological phase.

In conclusion, we studied two TO phonon modes in a set of $Pb_{1-x}Sn_xTe$ thin films across the trivial to TCI transition. We observed the occurrence of a ferroelectric phase in all the samples at a composition-dependent critical temperature. In that phase and under intense magnetic fields, the phonon modes exhibited circular polarization with opposite handedness. While the sample in the topologically trivial phase ($x = 0.24$) showed magnetic properties in agreement with a previous report for PbTe, the films in the TCI phase displayed unexpected results. First, a high degree of magnetic

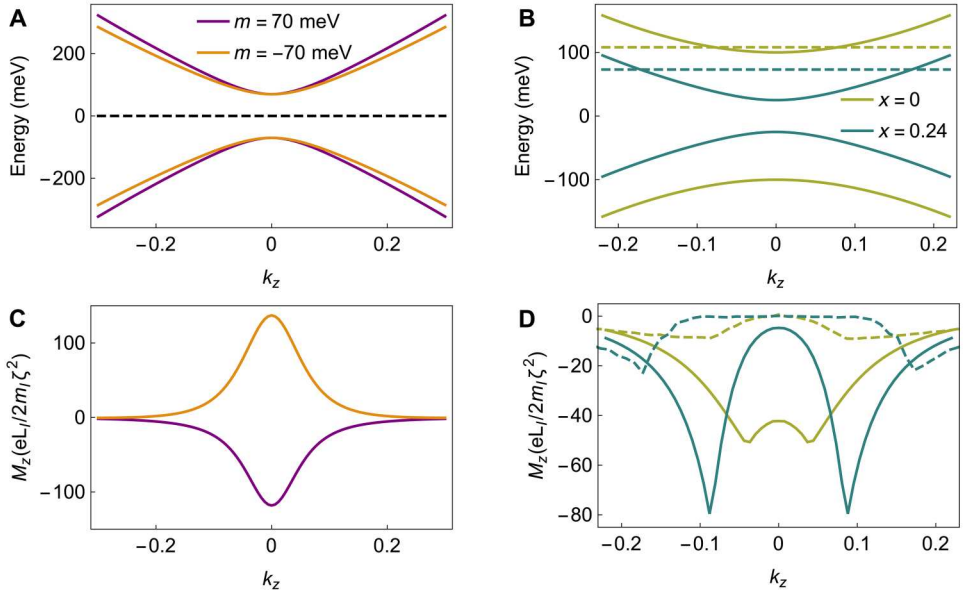

Fig. 4. Phonon magnetic moment from electronic band topology. (**A**) A generic electronic band structure for a *k*. *p* Hamiltonian describing the low energy bulk band structure in $Pb_{1-x}Sn_xTe$ for opposite mass terms with the Fermi level shown by a dashed line. (**B**) The band structure for the particular case of $x = 0$ and $x = 0.24$ where $v_F = 1$ eV, $v_3 = 0.3$ eV, and the Fermi level shown by the dashed line is calculated on the basis of carrier population. (**C**) Phonon magnetic moment calculated for the Fermi level in the gap for opposite mass terms. The phonon magnetic moment changes sign with the mass term. (**D**) The topological (solid) and nontopological (dashed) contribution to phonon magnetic moment for the two Sn concentrations in (B). The phonon magnetic moment from the two bands are equal and opposite, and thus, its value is suppressed when Fermi level lies below or above the gap.

circular dichroism could be reached at low magnetic fields. Second, the obtained effective *g*-factors for both phonons increased by two orders of magnitude and changed sign for the lowest-energy phonon mode across the topological transition, thus acquiring opposite signs between the modes. Furthermore, the diamagnetic shift showed an increase of one order of magnitude. These results demonstrate that the magnetic properties of phonons are largely enhanced in topological materials. Schemes for phonon manipulation with magnetic fields, with impact in properties such as thermal conductivity (*72*–*74*), can be more effectively applied in that phase of matter.

METHODS

Sample growth

The single-crystal $Pb_{1-x}Sn_xTe$ films were grown by molecular beam epitaxy, with a thickness of ~1.5 μm, on (111) BaF_2 substrates and with different Sn content across the topological phase transition. The hole concentrations were 1.7×10^{18}, 8.1×10^{18}, and 8.5×10^{18} cm^{-3} for the $x = 0.24$, 0.42, and 0.56 samples, respectively, deduced from Hall measurements. Extensive details of the growth parameters and magnetoconductivity results as a function of temperature, Sn content, and carrier density are shown in (*75*).

Measurements

The THz-TDS setup uses the output from a Ti:sapphire regenerative amplifier (1 kHz, 150 fs, and 775 nm; Clark-MXR Inc.) to generate pulsed terahertz radiation via optical rectification. For the magnetic field dependence of the phonon frequencies, we used the Rice Advanced Magnet with Broadband Optics setup. To avoid artifacts in the crossed configuration due to imperfections in the polarizers and to increase the signal-to-noise ratio, the measurements were repeated several times. See further experimental details in the Supplementary Materials.

Model for phonon magnetic moment of lead tin telluride

To calculate the band topology contribution to the phononic magnetic moment, we consider the following effective four-band low-energy Hamiltonian around the L point (*76*)

$$H_0 = (m + ck_3^2)\sigma_z + v_F(k_1 s_y - k_2 s_x)\sigma_x + v_3 k_3 \sigma_y \quad (1)$$

where k_1, k_2, and k_3 form an orthogonal system with k_3 pointing along ΓL line and k_1 along the [110] direction. The form of electron-phonon interaction, which is allowed by symmetry and results in a nonzero phonon magnetic moment, is given by

$$H_{ph} = \zeta(u_x s_0 \sigma_x - u_y s_z \sigma_y) \quad (2)$$

The phonon magnetic moment is then calculated by using equation 3 in (*28*)

$$M_z = \frac{e}{2m_I} L_I \int d\mathbf{k} \Omega_{k_x k_y u_x u_y} \quad (3)$$

where m_I is the mass of the representative ion with averaged angular momentum $L_I = (m_I/T)\int_0^T (\mathbf{u} \times \dot{\mathbf{u}})dt$ over the phonon period T, k_α, and u_α denote momentum and the displacement of phonon mode in α direction with second Chern form

$$\Omega_{\alpha\beta\gamma\delta} = \Omega_{\alpha\beta}\Omega_{\gamma\delta} + \Omega_{\beta\gamma}\Omega_{\alpha\delta} - \Omega_{\alpha\gamma}\Omega_{\beta\delta} \quad (4)$$

defined in terms of Berry curvature $\Omega_{\alpha\beta}$ in momentum ($\mathbf{k}$) and phonon displacement ($\mathbf{u}$) space.

Supplementary Materials

This PDF file includes:

Details of time-domain terahertz spectroscopy
Temperature dependence of the phonon frequencies
Fits of transmittance spectra
Phonon magnetic moment from electronic band topology
Figs. S1 to S10
Tables S1 to S3

REFERENCES AND NOTES

1. A. A. Maradudin, S. H. Vosko, Symmetry properties of the normal vibrations of a crystal. *Rev. Mod. Phys.* **40**, 1–37 (1968).
2. S. Streib, Difference between angular momentum and pseudoangular momentum. *Phys. Rev. B* **103**, L100409 (2021).
3. L. Zhang, Q. Niu, Angular momentum of phonons and the Einstein–de Haas Effect. *Phys. Rev. Lett.* **112**, 085503 (2014).
4. L. Zhang, Q. Niu, Chiral phonons at high-symmetry points in monolayer hexagonal lattices. *Phys. Rev. Lett.* **115**, 115502 (2015).
5. H. Zhu, J. Yi, M.-Y. Li, J. Xiao, L. Zhang, C.-W. Yang, R. A. Kaindl, L.-J. Li, Y. Wang, X. Zhang, Observation of chiral phonons. *Science* **359**, 579–582 (2018).
6. G. Grissonnanche, S. Thériault, A. Gourgout, M. E. Boulanger, E. Lefrançois, A. Ataei, F. Laliberté, M. Dion, J. S. Zhou, S. Pyon, T. Takayama, H. Takagi, N. Doiron-Leyraud, L. Taillefer, Chiral phonons in the pseudogap phase of cuprates. *Nat. Phys.* **16**, 1108–1111 (2020).
7. J. Medina Dueñas, H. L. Calvo, L. E. F. Foa Torres, Copropagating edge states produced by the interaction between electrons and chiral phonons in two-dimensional materials. *Phys. Rev. Lett.* **128**, 066801 (2022).
8. D. M. Juraschek, T. Neuman, P. Narang, Giant effective magnetic fields from optically driven chiral phonons in 4*f* paramagnets. *Phys. Rev. Res.* **4**, 013129 (2022).
9. D. Yao, S. Murakami, Chiral-phonon-induced current in helical crystals. *Phys. Rev. B* **105**, 184412 (2022).
10. G. Xiong, H. Chen, D. Ma, L. Zhang, Effective magnetic fields induced by chiral phonons. *Phys. Rev. B* **106**, 144302 (2022).
11. J. Bonini, S. Ren, D. Vanderbilt, M. Stengel, C. E. Dreyer, S. Coh, Frequency splitting of chiral phonons from broken time-reversal symmetry in CrI_3. *Phys. Rev. Lett.* **130**, 086701 (2023).
12. K. Ishito, H. Mao, Y. Kousaka, Y. Togawa, S. Iwasaki, T. Zhang, S. Murakami, J.-I. Kishine, T. Satoh, Truly chiral phonons in α-HgS. *Nat. Phys.* **19**, 35–39 (2023).
13. K. Ishito, H. Mao, K. Kobayashi, Y. Kousaka, Y. Togawa, H. Kusunose, J.-I. Kishine, T. Satoh, Chiral phonons: Circularly polarized Raman spectroscopy and ab initio calculations in a chiral crystal tellurium. *Chirality* **35**, 338–345 (2023).
14. C. P. Romao, R. Catena, N. A. Spaldin, M. Matas, Chiral phonons as dark matter detectors. arXiv:2301.07617 [hep-ph] (2023).
15. K. Kim, E. Vetter, L. Yan, C. Yang, Z. Wang, R. Sun, Y. Yang, A. H. Comstock, X. Li, J. Zhou, L. Zhang, W. You, D. Sun, J. Liu, Chiral-phonon-activated spin Seebeck effect. *Nat. Mater.* **22**, 322–328 (2023).
16. J. Luo, T. Lin, J. Zhang, X. Chen, E. R. Blackert, R. Xu, B. I. Yakobson, H. Zhu, Large effective magnetic fields from chiral phonons in rare-earth halides. arXiv:2306.03852 [cond-mat.mtrl-sci] (2023).
17. E. Anastassakis, E. Burstein, Morphic effects II-effects of external forces on the frequencies of the $\mathbf{q} \asymp 0$ optical phonons. *J. Phys. Chem. Solid* **32**, 563–570 (1971).
18. E. Anastassakis, E. Burstein, A. Maradudin, R. Minnick, Morphic effects-IV. Effects of an applied magnetic field on first-order photonoptical phonon interactions in non-magnetic crystals. *J. Phys. Chem. Solid* **33**, 1091–1103 (1972).
19. A. Baydin, F. G. G. Hernandez, M. Rodriguez-Vega, A. K. Okazaki, F. Tay, G. T. Noe, I. Katayama, J. Takeda, H. Nojiri, P. H. O. Rappl, E. Abramof, G. A. Fiete, J. Kono, Magnetic control of soft chiral phonons in PbTe. *Phys. Rev. Lett.* **128**, 075901 (2022).
20. G. Schaack, Observation of circularly polarized phonon states in an external magnetic field. *J. Phys. C Solid State Phys.* **9**, L297–L301 (1976).
21. B. Cheng, T. Schumann, Y. Wang, X. Zhang, D. Barbalas, S. Stemmer, N. P. Armitage, A large effective phonon magnetic moment in a Dirac semimetal. *Nano Lett.* **20**, 5991–5996 (2020).
22. D. M. Juraschek, M. Fechner, A. V. Balatsky, N. A. Spaldin, Dynamical multiferroicity. *Phys. Rev. Mater.* **1**, 014401 (2017).
23. D. M. Juraschek, N. A. Spaldin, Orbital magnetic moments of phonons. *Phys. Rev. Mater.* **3**, 064405 (2019).
24. R. M. Geilhufe, V. Juričić, S. Bonetti, J.-X. Zhu, A. V. Balatsky, Dynamically induced magnetism in $KTaO_3$. *Phys. Rev. Res.* **3**, L022011 (2021).
25. R. M. Geilhufe, W. Hergert, Electron magnetic moment of transient chiral phonons in $KTaO_3$. *Phys. Rev. B* **107**, L020406 (2023).
26. D. Bossini, D. M. Juraschek, R. M. Geilhufe, N. Nagaosa, A. V. Balatsky, M. Milanović, V. V. Srdić, P. Šenjug, E. Topić, D. Barišić, M. Rubić, D. Pajić, T. Arima, M. Savoini, S. L. Johnson, C. S. Davies, A. Kirilyuk, Magnetoelectrics and multiferroics: Theory, synthesis, characterisation, preliminary results and perspectives for all-optical manipulations. *J. Phys. D Appl. Phys.* **56**, 273001 (2023).
27. M. Basini, M. Pancaldi, B. Wehinger, M. Udina, T. Tadano, M. Hoffmann, A. Balatsky, S. Bonetti, Terahertz electric-field driven dynamical multiferroicity in SrTiO3. arXiv:2210.01690 [cond-mat.str-el] (2022).
28. Y. Ren, C. Xiao, D. Saparov, Q. Niu, Phonon magnetic moment from electronic topological magnetization. *Phys. Rev. Lett.* **127**, 186403 (2021).
29. R. M. Geilhufe, Dynamic electron-phonon and spin-phonon interactions due to inertia. *Phys. Rev. Res.* **4**, L012004 (2022).
30. T. H. Hsieh, H. Lin, J. Liu, W. Duan, A. Bansil, L. Fu, Topological crystalline insulators in the SnTe material class. *Nat. Commun.* **3**, 982 (2012).
31. Y. Tanaka, Z. Ren, T. Sato, K. Nakayama, S. Souma, T. Takahashi, K. Segawa, Y. Ando, Experimental realization of a topological crystalline insulator in SnTe. *Nat. Phys.* **8**, 800–803 (2012).
32. J. O. Dimmock, I. Melngailis, A. J. Strauss, Band structure and laser action in $Pb_xSn_{1-x}Te$. *Phys. Rev. Lett.* **16**, 1193–1196 (1966).
33. H. Kawamura, K. Murase, S. Nishikawa, S. Nishi, S. Katayama, Dielectric constant and soft mode of $Pb_{1-x}Sn_xTe$ by magnetoplasma reflection. *Solid State Commun.* **17**, 341–344 (1975).
34. K. L. I. Kobayashi, Y. Kato, Y. Katayama, K. F. Komatsubara, Carrier-concentration-dependent phase transition in SnTe. *Phys. Rev. Lett.* **37**, 772–774 (1976).
35. H. Burkhard, G. Bauer, A. Lopez-Otero, Submillimeter spectroscopy of to-phonon mode softening in PbTe. *J. Opt. Soc. Am.* **67**, 943–946 (1977).
36. S. Sugai, K. Murase, H. Kawamura, Observation of soft TO-phonon in SnTe by Raman scattering. *Solid State Commun.* **23**, 127–129 (1977).
37. C. W. Li, O. Hellman, J. Ma, A. F. May, H. B. Cao, X. Chen, A. D. Christianson, G. Ehlers, D. J. Singh, B. C. Sales, O. Delaire, Phonon self-energy and origin of anomalous neutron scattering spectra in SnTe and PbTe thermoelectrics. *Phys. Rev. Lett.* **112**, 175501 (2014).
38. M. P. Jiang, M. Trigo, I. Savić, S. Fahy, E. D. Murray, C. Bray, J. Clark, T. Henighan, M. Kozina, M. Chollet, J. M. Glownia, M. C. Hoffmann, D. Zhu, O. Delaire, A. F. May, B. C. Sales, A. M. Lindenberg, P. Zalden, T. Sato, R. Merlin, D. A. Reis, The origin of incipient ferroelectricity in lead telluride. *Nat. Commun.* **7**, 12991 (2016).
39. G. A. S. Ribeiro, L. Paulatto, R. Bianco, I. Errea, F. Mauri, M. Calandra, Strong anharmonicity in the phonon spectra of PbTe and SnTe from first principles. *Phys. Rev. B* **97**, 014306 (2018).
40. P. Chudzinski, Anharmonic coupling between electrons and TO phonons in the vicinity of a ferroelectric quantum critical point. *Phys. Rev. Res.* **2**, 012048(R) (2020).
41. K. A. U. Holm, N. Roth, C. M. Zeuthen, K. Tolborg, A. A. Feidenhans'l, B. B. Iversen, Temperature dependence of dynamic dipole formation in PbTe. *Phys. Rev. B* **102**, 024112 (2020).
42. R. D'Souza, J. Cao, J. D. Querales-Flores, S. Fahy, I. Savić, Electron-phonon scattering and thermoelectric transport in *p*-type PbTe from first principles. *Phys. Rev. B* **102**, 115204 (2020).
43. C. D. O'Neill, O. J. Clark, H. D. J. Keen, F. Mazzola, I. Marković, D. A. Sokolov, A. Malekos, P. D. King, A. Hermann, A. D. Huxley, Changes of Fermi surface topology due to the rhombohedral distortion in SnTe. *Phys. Rev. B* **102**, 155132 (2020).
44. C. S. Lent, M. A. Bowen, J. D. Dow, R. S. Allgaier, O. F. Sankey, E. S. Ho, Relativistic empirical tight-binding theory of the energy bands of GeTe, SnTe, PbTe, PbSe, PbS, and their alloys. *Superlattices Microstruct.* **2**, 491–499 (1986).
45. Y. Shi, M. Wu, F. Zhang, J. Feng, (111) surface states of SnTe. *Phys. Rev. B* **90**, 235114 (2014).
46. X. Li, F. Zhang, A. H. MacDonald, SU(3) Quantum Hall ferromagnetism in SnTe. *Phys. Rev. Lett.* **116**, 026803 (2016).
47. D. Varjas, M. Fruchart, A. R. Akhmerov, P. M. Perez-Piskunow, Computation of topological phase diagram of disordered $Pb_{1-x}Sn_xTe$ using the kernel polynomial method. *Phys. Rev. Res.* **2**, 013229 (2020).
48. A. K. Okazaki, S. Wiedmann, S. Pezzini, M. L. Peres, P. H. O. Rappl, E. Abramof, Shubnikov–de Haas oscillations in topological crystalline insulator SnTe(111) epitaxial films. *Phys. Rev. B* **98**, 195136 (2018).
49. B. Cheng, P. Taylor, P. Folkes, C. Rong, N. P. Armitage, Magnetoterahertz response and faraday rotation from massive Dirac fermions in the topological crystalline insulator $Pb_{0.5}Sn_{0.5}Te$. *Phys. Rev. Lett.* **122**, 097401 (2019).
50. J. Liu, W. Duan, L. Fu, Two types of surface states in topological crystalline insulators. *Phys. Rev. B* **88**, 241303 (2013).
51. S. Safaei, P. Kacman, R. Buczko, Topological crystalline insulator (Pb,Sn)Te: Surface states and their spin polarization. *Phys. Rev. B* **88**, 045305 (2013).

52. B. A. Assaf, T. Phuphachong, V. V. Volobuev, A. Inhofer, G. Bauer, G. Springholz, L. A. de Vaulchier, Y. Guldner, Massive and massless Dirac fermions in $Pb_{1-x}Sn_xTe$ topological crystalline insulator probed by magneto-optical absorption. *Sci. Rep.* **6**, 20323 (2016).
53. X. Gao, M. S. Daw, Investigation of band inversion in (Pb,Sn)Te alloys using ab initio calculations. *Phys. Rev. B* **77**, 033103 (2008).
54. S.-Y. Xu, C. Liu, N. Alidoust, M. Neupane, D. Qian, I. Belopolski, J. D. Denlinger, Y. J. Wang, H. Lin, L. A. Wray, G. Landolt, B. Slomski, J. H. Dil, A. Marcinkova, E. Morosan, Q. Gibson, R. Sankar, F. C. Chou, R. J. Cava, A. Bansil, M. Z. Hasan, Observation of a topological crystalline insulator phase and topological phase transition in $Pb_{1-x}Sn_xTe$. *Nat. Commun.* **3**, 1192 (2012).
55. J. Neu, C. A. Schmuttenmaer, Tutorial: An introduction to terahertz time domain spectroscopy (THz-TDS). *J. Appl. Phys.* **124**, 231101 (2018).
56. O. Delaire, J. Ma, K. Marty, A. F. May, M. A. McGuire, M.-H. Du, D. J. Singh, A. Podlesnyak, G. Ehlers, M. D. Lumsden, B. C. Sales, Giant anharmonic phonon scattering in PbTe. *Nat. Mater.* **10**, 614–619 (2011).
57. Z. Xiao, J. Wang, X. Liu, B. A. Assaf, D. Burghoff, Optical-pump terahertz-probe spectroscopy of the topological crystalline insulator $Pb_{1-x}Sn_xSe$ through the topological phase transition. *ACS Photonics* **9**, 765–771 (2022).
58. See Supplemental Material for details on the experimental methods and calculations of phonon magnetic moment from electronic band topology.
59. C. D. O'Neill, D. A. Sokolov, A. Hermann, A. Bossak, C. Stock, A. D. Huxley, Inelastic x-ray investigation of the ferroelectric transition in SnTe. *Phys. Rev. B* **95**, 144101 (2017).
60. C. Kittel, *Introduction to Solid State Physics* (John Wiley & Sons, ed. 8, 2005).
61. J. F. Scott, Soft-mode spectroscopy: Experimental studies of structural phase transitions. *Rev. Mod. Phys.* **46**, 83–128 (1974).
62. Y. Okamura, H. Handa, R. Yoshimi, A. Tsukazaki, K. S. Takahashi, M. Kawasaki, Y. Tokura, Y. Takahashi, Terahertz lattice and charge dynamics in ferroelectric semiconductor $Sn_xPb_{1-x}Te$. *npj Quantum Mater.* **7**, 91 (2022).
63. K. Kobayashi, Y. Kato, Y. Katayama, K. Komatsubara, Resistance anomaly due to displacive phase transition in SnTe. *Solid State Commun.* **17**, 875–878 (1975).
64. G. T. Noe, I. Katayama, F. Katsutani, J. J. Allred, J. A. Horowitz, D. M. Sullivan, Q. Zhang, F. Sekiguchi, G. L. Woods, M. C. Hoffmann, H. Nojiri, J. Takeda, J. Kono, Single-shot terahertz time-domain spectroscopy in pulsed high magnetic fields. *Opt. Express* **24**, 30328–30337 (2016).
65. A. Baydin, T. Makihara, N. M. Peraca, J. Kono, Time-domain terahertz spectroscopy in high magnetic fields. *Front. Optoelectron.* **14**, 110–129 (2021).
66. X. Li, K. Yoshioka, M. Xie, G. T. Noe, W. Lee, N. M. Peraca, W. Gao, T. Hagiwara, O. S. Handegård, L.-W. Nien, T. Nagao, M. Kitajima, H. Nojiri, C.-K. Shih, A. H. MacDonald, I. Katayama, J. Takeda, G. A. Fiete, J. Kono, Terahertz Faraday and Kerr rotation spectroscopy of $Bi_{1-x}Sb_x$ films in high magnetic fields up to 30 tesla. *Phys. Rev. B* **100**, 115145 (2019).
67. S. Yue, H. T. Chorsi, M. Goyal, T. Schumann, R. Yang, T. Xu, B. Deng, S. Stemmer, J. A. Schuller, B. Liao, Soft phonons and ultralow lattice thermal conductivity in the Dirac semimetal Cd_3As_2. *Phys. Rev. Res.* **1**, 033101 (2019).
68. X.-W. Zhang, Y. Ren, C. Wang, T. Cao, D. Xiao, Gate-tunable phonon magnetic moment in bilayer graphene. *Phys. Rev. Lett.* **130**, 226302 (2023).
69. Y. Liu, C.-S. Lian, Y. Li, Y. Xu, W. Duan, Pseudospins and topological effects of phonons in a Kekulé lattice. *Phys. Rev. Lett.* **119**, 255901 (2017).
70. Y. Liu, Y. Xu, S.-C. Zhang, W. Duan, Model for topological phononics and phonon diode. *Phys. Rev. B* **96**, 064106 (2017).
71. C. Lu, M. Zhang, H. Wang, Q. Ai, T. Liu, Topological quantum transition driven by charge-phonon coupling in higher-order topological insulators. *Phys. Rev. B* **107**, 125118 (2023).
72. T. Knittel, H. J. Goldsmid, Effect of magnetic field on the thermal conductivity of lead telluride-tin telluride. *J. Phys. C Solid State Phys.* **12**, 1891 (1979).
73. H. Jin, O. D. Restrepo, N. Antolin, S. R. Boona, W. Windl, R. C. Myers, J. P. Heremans, Phonon-induced diamagnetic force and its effect on the lattice thermal conductivity. *Nat. Mater.* **14**, 601–606 (2015).
74. J. He, T. M. Tritt, Advances in thermoelectric materials research: Looking back and moving forward. *Science* **357**, aak9997 (2017).
75. A. K. Okazaki, "Investigation of the magnetotransport properties in the crystalline topological insulator lead tin telluride," thesis, INPE, São José dos Campos (2019).
76. A. Lau, C. Ortix, Topological semimetals in the SnTe material class: Nodal lines and Weyl points. *Phys. Rev. Lett.* **122**, 186801 (2019).

Acknowledgments: We thank Y. Ren, D. Xiao, Q. Niu, and R. Matthias Geilhufe for useful discussions and G. T. Noe II and T. Makihara for assistance in measurements. **Funding:** This research was primarily supported by the NSF through the Center for Dynamics and Control of Materials: an NSF MRSEC under Cooperative Agreement No. DMR-1720595. F.G.G.H. acknowledges financial support from the Brasil@Rice Collaborative Grant, the São Paulo Research Foundation (FAPESP) grant nos. 2018/06142-5 and 2023/04245-0 and grant no. 409245/2022-4 of the National Council for Scientific and Technological Development (CNPq). P. H.O.R. and E.A. acknowledge support from CNPq nos. 307192/2021-0 and 302288/2022-8, respectively. G.A.F. acknowledges additional support from NSF DMR-2114825 and the Alexander von Humboldt Foundation. J.T. and I.K. acknowledge support from the Japan Society for the Promotion of Science (JSPS) (KAKENHI no. 20H05662). **Author contributions:** F.G.G.H. and J.K. conceived the project. F.G.G.H., A.B., and M.R.-V. lead the project and prepared the manuscript under the supervision of G.A.F. and J.K. F.G.G.H., A.B., and F.T. performed the measurements. F.G.G.H. and A.B. analyzed the experimental data. S.C. made the theoretical modeling under the supervision of M.R.-V. and G.A.F. I.K., J.T., and H.N. fabricated the pulsed magnet instrumentation. A.K.O., P.H.O.R., and E.A. grew the samples. All authors discussed the results and commented on the manuscript. **Competing interests:** The authors declare that they have no competing interests. **Data and materials availability:** All data needed to evaluate the conclusions in the paper are present in the paper and/or the Supplementary Materials.

Submitted 26 June 2023
Accepted 15 November 2023
Published 15 December 2023
10.1126/sciadv.adj4074